Water Research X 3 (2019) 100027

Contents lists available at ScienceDirect

Water Research X

journal homepage: https://www.journals.elsevier.com/water-research-x

# Reducing impedance to ionic flux in capacitive deionization with Bi-tortuous activated carbon electrodes coated with asymmetrically charged polyelectrolytes

Akash P. Bhat [a], Erik R. Reale [b], Martina del Cerro [a], Kyle C. Smith [b, c, d, e], Roland D. Cusick [a, *]

[a] Department of Civil and Environmental Engineering, University of Illinois at Urbana-Champaign, Urbana, IL, 61801, USA
[b] Department of Mechanical Science and Engineering, University of Illinois at Urbana-Champaign, Urbana, IL, 61801, USA
[c] Department of Materials Science and Engineering, University of Illinois at Urbana-Champaign, Urbana, IL, 61801, USA
[d] Computational Science and Engineering Program, University of Illinois at Urbana-Champaign, Urbana, IL, 61801, USA
[e] Beckman Institute for Advanced Study, University of Illinois at Urbana-Champaign, Urbana, IL, 61801, USA

ARTICLE INFO

*Article history:*
Received 19 November 2018
Received in revised form
22 February 2019
Accepted 23 February 2019
Available online 27 February 2019

*Keywords:*
Capacitive deionization
Polyelectrolyte coating
Bi-tortuous electrodes

ABSTRACT

Capacitive deionization (CDI) with electric double layers is an electrochemical desalination technology in which porous carbon electrodes are polarized to reversibly store ions. Planar composite CDI electrodes exhibit poor energetic performance due the resistance associated with salt depletion and tortuous diffusion in the macroporous structure. In this work, we investigate the impact of bi-tortuosity on desalination performance by etching macroporous patterns along the length of activated carbon porous electrodes in a flow-by CDI architecture. Capacitive electrodes were also coated with thin asymmetrically charged polyelectrolytes to improve ion-selectivity while maintaining the bitortuous macroporous channels. Under constant current operation, the equivalent circuit resistance in CDI cells operating with bi-tortuous electrodes was approximately 2.2 times less than a control cell with unpatterned electrodes, leading to significant increases in working capacitance (20–22 to 26.7–27.8 F $g^{-1}$), round-trip efficiency (52–71 to 71–80%), and charge efficiency (33–59 to 35–67%). Improvements in these key performance indicators also translated to enhanced salt adsorption capacity, rate, and most importantly, the thermodynamic efficiency of salt separation (1.0–2.0 to 2.2–4.1%). These findings demonstrate that the use of bi-tortuous electrodes is a novel approach of reducing impedance to ionic flux in CDI.


## 1. Introduction

Capacitive deionization (CDI) with electric double layers is an electrochemical desalination technology in which porous carbon electrodes are polarized at a constant current or voltage to decrease the salinity of water (Anderson et al., 2010; E. Suss et al., 2015; Porada et al., 2013). When discharged under constant current, regeneration of CDI salt removal capacity can be coupled to energy recovery (Długołęcki and van der Wal, 2013; Han et al., 2015; Tan et al., 2018; Zhao et al., 2012). A typical cell architecture involves the flow of feed solution in the channel created by the separation of porous carbon electrodes, called flow-by or flow-between CDI (fb-CDI) (Bouhadana et al., 2010; E. Suss et al., 2012; Porada et al., 2013). The simplicity of this architecture could translate to low system costs and fouling potential, however, the charge efficiency (ratio of charge equivalent of salt adsorbed to the charge input (Zhao et al., 2010)) and adsorption capacity remain low due to co-ion transport and repulsion (cation repulsion at the positive electrodes and vice-versa), as well as residual brine in the flow channel and electrode macropores preceding the discharge stroke (Suss et al., 2015; Kim and Choi, 2010; Li and Zou, 2011; Shang et al., 2017).

In fb-CDI cells, salt depletion occurs throughout the porous electrode leading to diffusional limitations, increased cell resistance during charging, and reverse flux of ions into the flow channel. This source of impedance impacts salt removal rate and capacity as well as the energy available for recovery during discharge. Ion-exchange membranes can be used to create a selective charge barrier to block co-ion transport and thereby

* Corresponding author.
*E-mail address:* rcusick@illinois.edu (R.D. Cusick).

https://doi.org/10.1016/j.wroa.2019.100027

**Nomenclature**

| | |
|---|---|
| $\eta_{CE}$ | Charge efficiency |
| $\eta_{FE}$ | Flow efficiency |
| $\eta_{RTE}$ | Round-trip efficiency |
| $\eta_{TE}$ | Thermodynamic efficiency with energy recovery |
| $\eta^{*}_{TE}$ | Thermodynamic efficiency without considering recovery |
| ASAR | Average salt adsorption rate, g $g^{-1}$ $min^{-1}$ |
| BT | Bi-tortuous |
| BT:0.8 V | Bi-tortuous electrodes charged till 0.8 V |
| BT:1.0 V | Bi-tortuous electrodes charged till 1.0 V |
| BT:1.2 V | Bi-tortuous electrodes charged till 1.2 V |
| $c_B$ | average brine concentration in throughout the discharge stroke, mol $L^{-1}$ |
| $c_D$ | average desalinated stream concentration throughout the charge stroke, mol $L^{-1}$ |
| CDI | Capacitive deionization |
| $C_{eff}$ | effluent concentration mol $L^{-1}$ |
| $C_{feed}$ | influent stream concentration mol $L^{-1}$ |
| $D_0$ | Bulk diffusivity |
| $D_{eff}$ | Effective ionic diffusivity |
| EDS | Energy Dispersive X-ray spectroscopy |
| $E_{in}$ | Energy transferred to the cell during the charge stroke, J |
| ENAS | Energy normalized adsorbed salt with energy recovery, mol $J^{-1}$ |
| ENAS* | Energy normalized adsorbed salt without considering recovery, mol $J^{-1}$ |
| $E_{out}$ | Energy obtained from the cell during the discharge stroke, J |
| ESR | Equivalent series resistance, Ω |
| F | Faraday's constant (96385.3), C $mol^{-1}$ |
| Fb-CDI | Flow-by capacitive deionization |
| M | molar mass of the salt, g $mol^{-1}$ |
| m | total mass of both the electrodes, g |
| $M_c$ | MacMullin number |
| MCDI | Membrane capacitive deionization |
| NMP | N-methyl-2-pyrrolidone |
| PDADMAC | poly(diallyldimethylammonium chloride) |
| PSS | poly(sodium 4-styrenesulfonate) |
| PVDF | polyvinylidene fluoride |
| Q | Volumetric flowrate of the influent stream, L $s^{-1}$ |
| $q_{in}$ | Charge transferred to the cell during the charge stroke, C |
| R | Universal gas constant (8.31446), J $mol^{-1}$ $K^{-1}$ |
| SAC | Salt adsorption capacity, g $g^{-1}$ |
| SEM | Scanning electron microscopy |
| T | Temperature, K |
| $t_c$ | Charging time, s |
| $t_{cycle}$ | Total cycle time, s |
| UP | Unpatterned |
| UP:0.8 V | Unpatterned electrodes charged till 0.8 V |
| ε | Porosity of the electrode |
| $\varepsilon_{FC}$ | Porosity of the flow channe separator |
| $K_0$ | Bulk conductivity |
| $K_{eff}$ | Effective ionic conductivity |
| τ | Tortuosity |
| $\tau_c$ | Residence time of the reactor, s |
| $\Delta N_{eff}$ | Moles of salt removed from the feed stream during a charging cycle, mol |
| $\Delta g_{sep}$ | Minimum Gibbs free energy of separation, J |
| γ | Water recovery or the fraction of feed stream that has been desalinated during the total cycle |

improve the charge efficiency (Biesheuvel and van der Wal, 2010; Lee et al., 2006; Li et al., 2008), but membrane cost is potentially prohibitive (Biesheuvel and van der Wal, 2010). Alternatively, electrodes can be coated with charged polyelectrolytes or fabricated with charged binders to cover macropores ion-selective layer of low resistance to retain co-ions (Ahualli et al., 2017; Kim et al., 2019b). While polyelectrolyte coating could serve as a cost-effective means promoting counter ion flux into and out of electric double layers, it remains unclear if selectivity enhancements observed under constant voltage charging would hold under constant current operation, in which charge efficiency is limited by salt residue from preceding discharge strokes (Hawks et al., 2018; Shang et al., 2017).

In addition to establishing ion-selective layers, significant efforts have been made to expand the design landscape of CDI architecture. One such architecture is flow-through CDI (ft-CDI), which involves the flow of solution through the porous electrode parallel to the applied field. Ft-CDI requires the use of monolithic electrodes with multi-scale pores to enable advective flow through the electrode macropores and salt adsorption within micropores (E. Suss et al., 2015; Guyes et al., 2017). This electrode architecture enables a reduction in ion diffusion length due to advection, increasing the diffusion kinetics as compared to fb-CDI. A foundational study by on ft-CDI demonstrated a 4 to 10 times increase in the sorption rate as compared to fb-CDI, with a mean sorption rate of 1 mg $g^{-1}$ $min^{-1}$ (E. Suss et al., 2012). Laser perforation within the ft-electrode macrostructure have been shown to enhance the permeability due to an increase in macroporosity (E. Guyes et al., 2017). Ft-CDI, however could have higher faradaic reactions leading to anode oxidation (Remillard et al., 2018), and flowing through the electrode could incur elevated pumping energy requirements due to head loss in the electrodes.

There have been studies on effect of the composite electrode design on CDI cell performance. Previous studies have demonstrated that a decrease in electrode thickness increases the rate of sorption, and that thicker electrodes had higher desalination times without affecting the energy consumed per mol of salt adsorbed (Dykstra et al., 2016; Kim and Yoon, 2015). Etching patterns in the electrode macrostructure has been shown to enhance the energy storage performance of capacitive and insertion electrodes by increasing effective ionic conductivity and creating a bi-tortuous (BT) electrolyte diffusion pathway (Bae et al., 2013; Cobb and Blanco, 2014; Cobb and Solberg, 2017; Nemani et al., 2015; Reale and Smith, 2018; Reale and Smith, 2018, 2018). BT electrodes have not been studied yet for their desalination performance. Reduction in tortuosity by introducing macropores could significantly reduce the resistance and increase the capacitance of the cell, thereby enhancing the performance of fb-CDI cells. Utilizing BT electrodes in CDI could also improve the thermodynamic efficiency by improving energy recovery and reducing the impacts of salt residue on charge efficiency. In the present work, the performance of bi-tortuous electrodes in an fb-CDI cell is tested in constant current operation and is compared to that of conventional unpatterned electrodes. Asymmetrically charged polyelectrolytes were adsorbed onto the electrode films to provide charge selectivity and to maintain the patterned macroporous electrode structure. The objective of this study is to demonstrate the effect of bi-tortuosity on various CDI cell performance metrics at various current

densities and cut-off voltages.

## 2. Materials and methods

### 2.1. Electrode fabrication

Electrodes were prepared as described previously (Reale and Smith, 2018). Briefly, YP-50 activated carbon (Kuraray Corporation, Japan) was used as the capacitive material. Electrode slurry was prepared by mixing 0.85 g of YP-50 activated carbon, 0.05 g of C45 carbon black, as a conductivity additive, and 0.1 g polyvinylidene fluoride (PVDF, Millipore Sigma, United States) binder. One gram of solid material was dissolved in 3 mL of N-methyl-2-pyrrolidone (NMP, Millipore Sigma, United States) solvent. The container was sealed, and the slurry was mixed for 15 min using the standard mode of operation for the Thinky ARE-310 planetary mixer to ensure thorough mixing, followed by 5 min on the deaeration setting to ensure removal of air bubbles. Electrodes were cast into a well carved within a graphite current collector ($L \times W \times H$: 3 cm × 0.5 cm × 0.25 mm) using a film applicator (Elcometer, United Kingdom). The cast electrodes were submerged in deionized water for wet phase inversion for 1 h to allow water to replace NMP. The electrodes were air-dried at 22 °C for at least 2 h to allow the water and dilute NMP to evaporate.

Two types of electrodes were prepared for the study: unpatterned (UP) and bi-tortuous (BT). Bi-tortuous electrodes were prepared by machining the unpatterned electrodes with macroporous patterns. Macropores were cut using a 100 μm diameter flat micro-mill (Harvey Tool Company, United States) at a spindle speed of 1200 rpm and one inch per minute, as previously described (Reale and Smith, 2018). The depth of the macropores was targeted at >75% of the electrode thickness, a precision limit placed by the macro-mill used, which had a resolution of 25 μm. Based on previous studies and simulations, the spacing of the macropores covered 25% of the electrode area (Nemani et al., 2015; Reale and Smith, 2018). The electrodes were immersed in deionized water to wet the microstructure and to remove any air bubbles. Scanning electron microscopy (SEM) was used to characterize the top view of the macropore patterns and compare them to unpatterned electrodes (Fig. 1).

### 2.2. Polyelectrolyte coating

Charged polyelectrolytes were adsorbed onto porous carbon films in the present study not only to introduce ion-selectivity at the electrode/flow-channel diffusion interface but also to maintain the macroporous profiled structure of bi-tortuous electrodes (Ahualli et al., 2017). Polyelectrolyte coating was formed by submerging the negative and positive electrodes, respectively, in 100 mM solution of poly(diallyldimethylammonium chloride) (PDADMAC, Molecular weight <100,000, Millipore Sigma, United States) and poly(sodium 4-styrenesulfonate) (PSS, Molecular weight ~ 200,000, Millipore Sigma, United States) for 24 h followed by drying over-night. The presence of the coating was confirmed by elemental mapping of a cross-section of coated electrodes using Energy Dispersive X-ray Spectroscopy (EDS) for presence of sodium and sulfur for PSS, and chlorine for PDADMAC. (Fig. 1). For the cross-sectional images, samples were frozen in liquid nitrogen before sectioning.

### 2.3. Experimental setup and desalination experiments

Two fb-CDI cells, one containing two unpatterned electrodes and the other containing two bi-tortuous electrodes, each coated with polyelectrolytes, were used for the desalination experiments (Fig. 1C and D). Uncoated bi-tortuous and uncoated unpatterned electrode cells were also evaluated but due to poor performance caused by co-ion repulsion (Table 2) our analysis focused on polyelectrolyte coated electrodes. Composite activated carbon electrodes were cast into a well etched within a graphite current collector with a 0.25 mm thickness and a projected area of 1.5 $cm^2$ ($L \times W$: 3 cm × 0.5 cm). There was a reduction in electrode mass due to the etching of macrochannels. The area normalized mass of the bi-tortuous electrodes (both anode and cathode) was 14.27 mg $cm^{-2}$, while that of both the unpatterned electrodes was 15.67 mg $cm^{-2}$. Within the flow cell, electrodes were separated using a glass microfiber separator (porosity $\varepsilon_{FC} = 0.7$ and thickness = 250 μm) and the flow channel was sealed using a gasket of 125 μm thickness. The feed solution (50 mM deaerated NaCl) was pumped through the cell at a flow rate of 0.2 mL per minute using a syringe pump (Harvard Apparatus, Holliston, MA). Effluent concentration was calculated by using a conductivity calibration curve. Effluent conductivity was measured using an in-line conductivity flow cell (ED916, eDAQ, Australia). Experimental residence time in unpatterned and bi-tortuous flow cells were measured by an NaCl tracer test using a pulse input method by measuring the effluent conductivity and were 32 s and 12 s for the bi-tortuous and unpatterned cell respectively. The residence time for the bi-tortuous electrode cell was higher than unpatterned because of the added volume created by etching the macropores. Residence

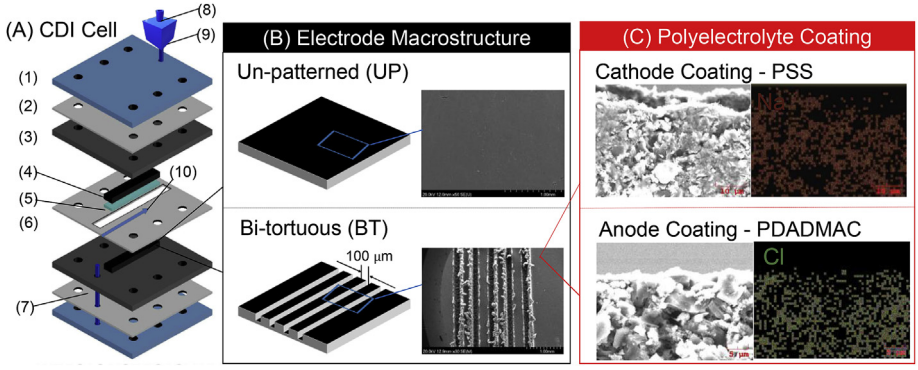


**Fig. 1.** (A) Separated layers as used in the construction of the CDI flow cell with (1) Acrylic end plates, (2) End plate sealing gasket, (3) Graphite current collector, (4) Activated carbon electrodes, (5) Porous glass fiber spacer, (6) flow-channel separator, (7) Flow in, (8) Effluent conductivity probe (9) Flow out, (10) flow direction through the flow-channel. (B) Graphical and SEM images of view of the un-patterned (UP) and bi-tortuous (BT) electrode evaluated in the flow cell, (C) Cross-sectional SEM image of the cathode electrode coated cation exchange polyelectrolyte (PSS) and anode electrode coated with anion exchange polyelectrolyte (PDADMAC). Distribution of coating was confirmed with EDS elemental mapping of Sodium and Chlorine.

times in the reactors were used for the calculation of flow efficiency described in the next section (Hawks et al., 2018).

During desalination cycling experiments, the fb-CDI cells were charged and discharged at constant current densities of (±) 5, 10, 12, 15, 20 and 25 A $m^{-2}$ normalized to the projected area of the electrodes (1.5 $cm^2$) using a galvanostat (Bio-Logic Inc., France). Constant current (CC) operation was utilized rather than constant voltage (CV) to assess the impact of BT electrodes on round trip energy efficiency and net energy consumption (Qu et al., 2016). The cell was charged until a specified cut-off voltage was reached followed by reversing cell current at equal density until the voltage reached 0 V. The charge and discharge cycles immediately followed each other with no time in between for hydraulic flushing. Comparison between unpatterned (UP) and bi-tortuous (BT) electrodes was performed with a cut-off voltage of 0.8 V (UP:0.8 V and BT:0.8 V) including the use of a duplicate set of electrodes. The cut-off voltage was kept at 0.8 V to eliminate any faradaic and parasitic reactions that could affect the electrode performance. The performance of bi-tortuous electrodes was further tested for cut-off voltages of 1.0 V and 1.2 V (BT:1.0 V and BT:1.2 V). A minimum of 10 cycles were run for each condition. Data were analyzed after a minimum of 5 continuous cycles once steady state had been reached (the length and depth of desalination curves did not change). At least four curves within the dynamic steady state were analyzed and averaged. Error bars indicate one standard deviation above and below the mean respectively. Uncoated electrodes (UP uncoated and BT uncoated) were tested at a current density of 10 A $m^{-2}$ and voltage window of 0.8 V for comparison to the polyelectrolyte coated electrodes.

Electrochemical impedance spectroscopy (EIS) was performed to characterize differences in resistance, tortuosity, and capacitance between unpatterned and bi-tortuous electrodes and to demonstrate the impact of polyelectrolyte coating. Potentiostatic EIS scan was performed from 100 KHz to 10 mHz with 6 points analyzed per decade. Three EIS scans were analyzed to report the mean and standard deviation. MacMullin number ($M_c$) directly relates to tortuosity and was determined by fitting the EIS data to the transmission-line model as given in the previous study for bi-tortuous electrodes (Reale and Smith, 2018).

$$\frac{K_{eff}}{K_0} = \frac{1}{M_c} = \frac{\varepsilon}{\tau},\ where\ K_{eff} = \frac{K_0.\varepsilon}{\tau},\ and\ D_{eff} = \frac{D_0.\varepsilon}{\tau} \quad (1)$$

Where $K_{eff}$ is the effective ionic conductivity, $K_0$ is the bulk conductivity, $M_c$ is the MacMullin number, $\varepsilon$ is the porosity, $\tau$ is the tortuosity, $D_{eff}$ is the effective ionic diffusivity and $D_0$ Is the bulk diffusivity (Thorat et al., 2009).

### 2.4. Performance metrics and calculations

The performance of CDI cells with unpatterned and bi-tortuous electrodes was characterized in terms of both capacitive energy storage and desalination. The equivalent series resistance (ESR in Ω $cm^2$) of the cells was calculated by dividing the initial increase cell voltage by the current density (Chen et al., 2018). Capacitance was measured from the slope of the voltage discharge curve. The applied current was divided by the slope and then normalized by the total electrode mass to obtain capacitance (F/g). Round trip efficiency ($\eta_{RTE}$, Equation (2)) of the charge/discharge cycle was calculated as the ratio of energy recovered during the discharge cycle ($E_{out}$) to the energy passed during the charging cycle ($E_{in}$) (Suss et al., 2015).

$$\eta_{RTE} = \frac{E_{out}}{E_{in}} \quad (2)$$

Salt adsorption capacity (SAC, mg $g^{-1}$) was determined by integrating the charge curve of the effluent concentration profile and normalizing salt removal to the mass of both electrodes.

$$\Delta N_{eff} = \int_{tcycle} Q\left(C_{feed} - C_{eff}\right)dt\ where\ Q\left(C_{feed} - C_{eff}\right) > 0 \quad (3)$$

Here $\Delta N_{eff}$ is the moles of salt removed from the feed stream during a charging cycle, $Q$ is the volumetric flowrate of the influent in L $s^{-1}$, $C_{feed}$is the concentration of the feed or influent in mol $L^{-1}$, $C_{eff}$ is the concentration of the effluent in mol $L^{-1}$ and $t_{cycle}$ is the total cycle time in seconds (Hawks et al., 2018).

$$SAC = \frac{M.\Delta N_{eff}}{m} \quad (4)$$

Here $M$ is the molar mass of the salt (58.44 g $mol^{-1}$ for NaCl) and $m$ is the total mass of the electrodes in g.

Average salt adsorption rate (ASAR) was determined by dividing the salt adsorbed during charging by the total cycle time, and then normalized to total electrode mass.

$$ASAR = \frac{M.\ \Delta N_{eff}}{m.t_{cycle}} \quad (5)$$

Observed charge efficiency ($\eta_{CE}$), which relates the effective charge adsorbed to the total charge passed in the circuit during charging, incorporates losses due to faradaic reactions, co-ion repulsion during electrosorption, desalination of brine residue in the flow-channel and electrode from the previous cycle (Shang et al., 2017). Charge efficiency was calculated as a ratio of charge equivalent of salt removed to the total charge passed during charging.

$$\eta_{CE} = \frac{\Delta N_{eff}.F}{q_{in}} \quad (6)$$

Here $F$ is the Faraday's constant (96,385.3 C $mol^{-1}$) and $q_{in}$ is the charge transferred to the cell during the charge stroke in Coulombs.

Flow efficiency ($\eta_{FE}$) is a parameter that influences observed charge efficiency, and captures losses due to the non-recoverable portion of desalinated water inside the reactor as well as other losses due to mixing (Hawks et al., 2018). Flow efficiency was calculated with no flush conditions using the time spent in charging ($t_c$, experimental) for different current densities and the cell residence time ($\tau_c$, section 2.4) according to the procedure given in Hawks et al. (equation (7)) (Hawks et al., 2018).

$$\eta_{FE} = \frac{2.\tau_c}{t_c}\ln\left(\frac{e^{\frac{\tau_c}{t_c}} + 1}{2}\right) - 1 \quad (7)$$

The energy efficiency of desalination was quantified using energy-normalized adsorbed salt (ENAS) and thermodynamic efficiency to relate moles of salt adsorbed ($\Delta N_{eff}$) and energy consumed by the cell. The values of energy consumed used for the determination of energy-normalized adsorbed salt (ENAS) and thermodynamic efficiencies were calculated by: i) considering only the energy consumed during the charging cycle (without recovery) and ii) accounting for the energy during cell discharge (with recovery). ENAS was calculated as the amount of salt removed normalized to the energy consumed with and without recovery (Equation (8) and (9)) (Hemmatifar et al., 2016).

$$ENAS^{*} = \frac{\Delta N_{eff}}{E_{in}} \ (Without\ recovery) \tag{8}$$

$$ENAS = \frac{\Delta N_{eff}}{E_{in} - E_{out}} \ (With\ recovery) \tag{9}$$

Thermodynamic efficiency was calculated as the ratio of the minimum thermodynamic energy to the actual energy consumed with and without recovery (Equations (11) and (12)) (Długołęcki and van der Wal, 2013). The minimum thermodynamic energy for each desalination run was calculated as the minimum theoretical work required to separate the influent stream into dilute stream (desalinated) and concentrated streams (brine) using the influent, brine and desalinated stream concentrations in the equation given below (Equation (10)) (Biesheuvel, 2009; Długołęcki and van der Wal, 2013).

$$\Delta g_{sep} = 2RT\left[c_D ln c_D + \left(\frac{1}{\gamma} - 1\right) c_B ln c_B - \frac{c_{feed}}{\gamma} ln c_{feed}\right] \tag{10}$$

Here $\Delta g_{sep}$ is the minimum thermodynamic energy required to separate the influent stream into desalinated and brine streams respectively. $c_D$ and $c_B$ are average effluent stream concentration after the charge cycle and discharge cycle respectively. $R$ is the universal gas constant (8.314 J mol$^{-1}$ K$^{-1}$), $T$ is the temperature in Kelvin and $\gamma$ is the water recovery or the fraction of volume of feed passed during the total cycle which has been desalinated during the charge cycle.

$$\eta_{TE}^{*} = \frac{\Delta g_{sep}}{E_{in}} \ (Without\ recovery) \tag{11}$$

$$\eta_{TE} = \frac{\Delta g_{sep}}{E_{in} - E_{out}} \ (With\ recovery) \tag{12}$$

## 3. Results and discussion

### 3.1. Effect of bi-tortuosity on capacitance, resistance, and round-trip energy efficiency

The introduction of macro-porous channels increased the effective ionic conductivity within BT electrodes, resulting in an average of 27% higher observed capacitance and a 56% lower equivalent circuit resistance (Fig. 2A and B). The ratio of bi-tortuous to unpatterned cell capacitance, as measured from the slope of the discharge stroke, at a charging cut-off voltage of 0.8 V ranged from 1.21 at 5 A m$^{-2}$ to 1.32 at 25 A m$^{-2}$. Raising the charging cut-off voltage for bi-tortuous electrodes to 1.0 and 1.2 V increased capacitance at lower current densities but also increased ESR by an average of 80% and the rate of capacity decay as operating current increased.

The reduction in the equivalent circuit resistance in etched electrodes provides evidence that the ionic conductivity was higher in BT electrodes. Alignment of ESR values for unpatterned and bi-tortuous electrodes can be seen with the real impedance values from EIS plots (Fig. S2). Bi-tortuous electrodes showed significantly lower ohmic resistance (high frequency region) as compared to their unpatterned counterparts (Fig. S2). Tortuosity is proportional to MacMullin number, which can be determined by fitting the EIS data into the analytical version of the transmission-line model given in the previous study (Reale and Smith, 2018). MacMullin numbers were determined for uncoated electrodes using the above-mentioned model and were found to be 6.4 ± 0.15 and 8.2 ± 0.07 for bi-tortuous and unpatterned electrode cells respectively. A reduction in MacMullin number indicates a reduction in tortuosity for bi-tortuous electrodes. The MacMullin numbers for polyelectrolyte coated electrodes could not be determined because of the overlap between electrode and charged polymer elements in the EIS in the mid-frequency region (Fig. S2) (Cusick et al., 2013; Długołęcki et al., 2010). The observed increase in ESR at higher voltage windows could be caused by both faradaic reactions and ohmic resistance (Fig. 2B). At higher voltage windows, the transition of current from capacitive to faradaic leads to an increase in leakage current at low current densities due to longer charging times (Shang et al., 2017). At low current densities, faradaic reactions (e.g. water splitting, oxygen reduction and carbon corrosion) occurring at higher voltage windows would cause pH gradients to establish leading to a more significant initial voltage jump (Zhang et al., 2019). When charged at higher current densities, a more significant concentration gradient across the polyelectrolyte ion-selective diffusion interface, and associated Donnan potential, may have contributed to the ESR and the capacity decay.

Enhancing energy recovery, or round-trip efficiency, has been shown to improve specific energy consumption of deionization (Długołęcki and van der Wal, 2013; Dykstra et al., 2018). The round-trip efficiencies observed for CDI cells with bi-tortuous electrodes charged at 0.8 V (BT:0.8V) remained consistently high at all the operating current densities (Fig. 2C). Between 71 and 80% of energy

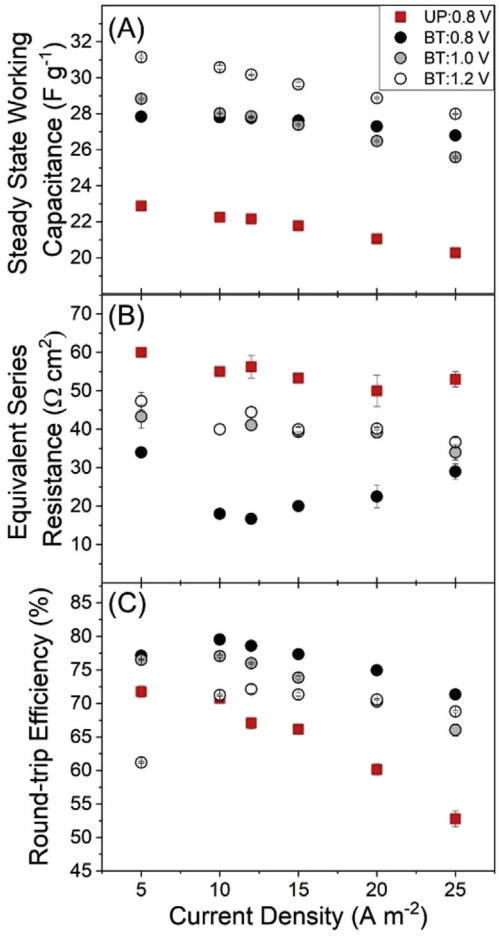


**Fig. 2.** (A) Steady state working capacitance calculated the discharge stroke of galvanostatic operation, (B) Equivalent Series Resistance (ESR) polyelectrolyte coated electrodes and (C) Percentage round trip energy efficiency or energy recovery for Unpatterned (UP) and Bi-tortuous (BT) as a function of current density.

consumed during the desalination charge stroke could be recovered during the discharge cycle for the BT electrodes, whereas the round-trip efficiencies for the unpatterned electrodes were between 52 and 71%. The bi-tortuous electrodes had lower resistive energy losses due to a reduction in equivalent series resistance, increasing both, the amount of energy that is stored and recoverable as compared to UP electrodes. Increasing the cut-off charging voltage of bi-tortuous electrodes to 1.0 and 1.2 V led to slightly lower observed $\eta_{RTE}$ (Fig. 2C). While the trends in $\eta_{RTE}$ were similar for 0.8 and 1.0 V, charging the bi-tortuous electrodes to 1.2 V at lower current densities caused a steep decline the recoverable energy. This is likely due to a transition from capacitive to faradaic current above 1.0 V. The curvature observed in the voltage and SAC profiles of the bi-tortuous electrodes charged at 1.2 V provide qualitative evidence for the transition toward faradaic current (Fig. 3E and F).

Round trip efficiencies for the bi-tortuous electrodes compare favorably with previous studies on MCDI systems despite the fact that there will be depletion within the electrode structure as compared to no depletion in MCDI when covered with IEMs. Previous studies on CDI systems have reported round-trip efficiencies up to 65% (García-Quismondo et al., 2013; 2016). For fb-MCDI, Zhao et al. previously reported approximately 15–40% round-trip efficiency at current densities higher than 25 A $m^{-2}$. In other studies, Długołęcki and van der Wal (2013) observed a rapid reduction in round-trip efficiency from 80 to 20% and Kim et al. (2019a,) also observed a reduction in round-trip efficiency from 70% to 45% at much lower current densities (2–10 A $m^{-2}$). These declines were very similar to that of UP electrodes. While electrode depletion is not expected for MCDI, the use of discrete membranes introduces additional ohmic and diffusive impedance, which may have limited round-trip efficiency in these studies (Cusick et al., 2013; Długołęcki et al., 2010a). These findings highlight how both the BT electrode macrostructure and polyelectrolyte coating promoted energy recovery while enhancing salt removal performance.

### 3.2. Effect of bi-tortuosity on charging time, salt adsorption capacity, and rate

The higher working capacitance of bi-tortuous electrodes also translated to improvements in salt adsorption capacity and rate (Figs. 3 and 4). Despite having less active material than UP electrodes, due to the creation of macrochannels, the charging times for the bi-tortuous electrodes at 0.8 V were 14.4% longer at 5 A $m^{-2}$ to 23.8% longer at 25 A $m^{-2}$ leading to a greater amount of salt adsorbed per charge stroke (Fig. 3). The maximum salt adsorption capacity (SAC) was an average of 42–68% higher for the bi-tortuous electrodes (4.1–9.7 mg $g^{-1}$) as compared to their unpatterned counterparts (2.4–6.8 mg $g^{-1}$) (Fig. 4). Despite longer cycle times, the average salt adsorption rate (ASAR) for the bi-tortuous electrodes was also 21% greater (Fig. 4), implying that the macrochannels increased the rate of diffusive flux into and out of the carbon films. While the tortuosity of polyelectrolyte coated

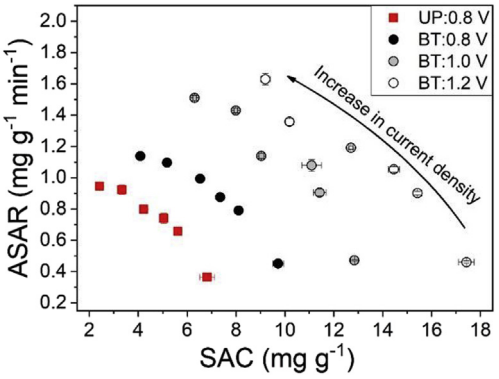


**Fig. 4.** Kim-Yoon plot for unpatterned electrodes at a voltage cut-off of 0.8 V and bi-tortuous electrodes at voltage cut-offs of 0.8, 1.0, and 1.2 V. The plot shifts towards the upper-right corner by the use of bi-tortuous electrodes, indicative of an increase in SAC and ASAR both.

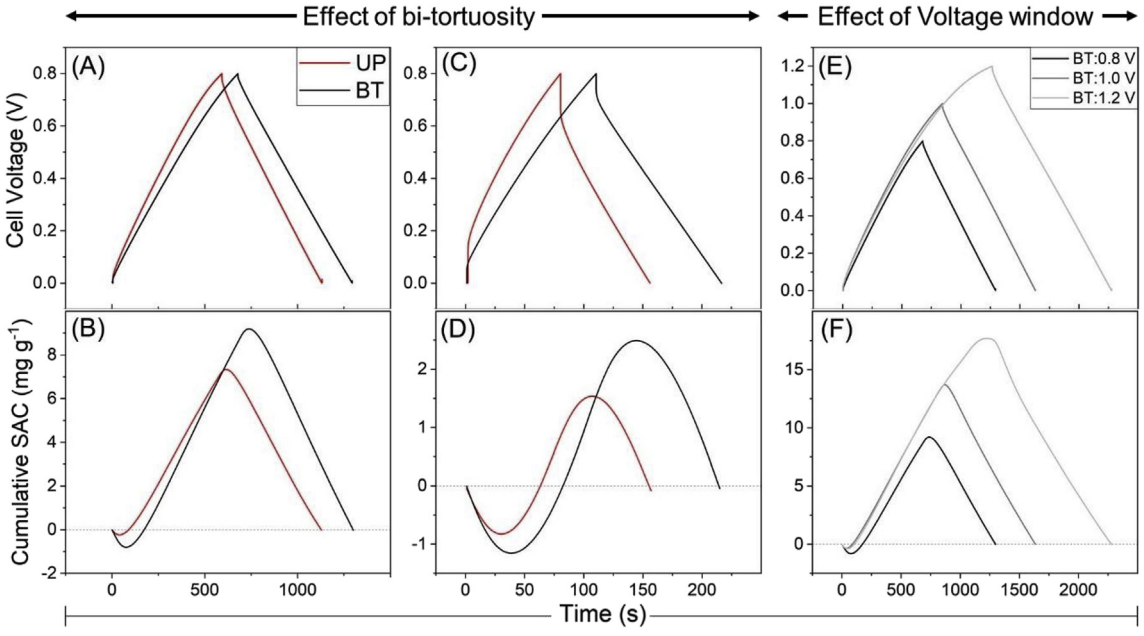


**Fig. 3.** Representative charge-discharge voltage profiles for unpatterned (UP) and bi-tortuous (BT) electrodes and corresponding cumulative SAC profiles for 0.8 V cut-off and 5 A $m^{-2}$ (A and B), for 0.8 V cut-off and 25 A $m^{-2}$ (C and D), and BT electrodes for different cut-off voltages of 0.8 V, 1 V, and 1.2 V cut-off at 5 A $m^{-2}$ (E and F). The charging time for BT electrodes is higher than UP electrodes due to increased capacitance, leading to an increase salt adsorption.

electrodes could not be accurately modeled using a three-element equivalent circuit transmission-line modeling, the increase in flux can be clearly observed in the cumulative SAC for each condition (Fig. 3). Further comparing different cut-off voltages at 5 A $m^{-2}$, the charging times for BT electrodes charged at 0.8, 1.0, and 1.2 V were 1,298 ± 3, 1,635 ± 1 and 2,275 ± 1 s respectively (Fig. 3), leading to the highest salt adsorption of 17.4 ± 0.31 mg $g^{-1}$ 1.2 V (Fig. 4).

Despite the observance of reverse ionic flux and faradaic reactions (Fig. S1), the rate and capacity of salt adsorption for polyelectrolyte coated BT electrodes compared favorably with previous constant current MCDI studies (Table 1). Improvements in diffusion kinetics and sorption rate for BT electrodes due to the presence of macroporous channels are similar to ft-CDI electrodes without having to use highly macroporous specialized monolithic electrodes. The 20% increase in sorption rate for BT electrodes is less than, yet comparable to the increase in rate by using ft-CDI. Previous studies have demonstrated a 4 to 10 times increase in sorption rate in ft-CDI cells as compared to their fb-CDI counterparts (E. Suss et al., 2012). While in ft-CDI architecture, advection through the macropores is used to overcome diffusional limitations to increase the sorption rate, BT-CDI electrodes uses macropores to increase ionic conductivity by reducing the effective diffusion length.

### 3.3. Effect of bi-tortuous electrodes on charge and energy efficiency

Co-ion repulsion was observed for uncoated electrodes, and as expected, adding polyelectrolyte coatings improved charge and energy efficiency for both UP and BT electrodes (Ahualli et al., 2014, 2017). Polyelectrolyte coatings significantly improved the performance for both UP and BT electrodes by retaining co-ions within the electrode macropores (Table 2). Desalination capacity was highest for BT electrode coated with asymmetrically charged polyelectrolytes due to the synergistic effect of reduced impedance and ion-selectivity. However, improvements in $\eta_{CE}$ were significantly lower than previously reported values for electrodes with distributed fixed charge (e.g. charged carbon, charged binder, and polyelectrolyte coating) that were operated under constant voltage (Gao et al., 2015; 2016; M. Kim et al., 2019b) due to flow efficiency losses commonly associated with constant current operation of CDI cells (Hawks et al., 2018).

The charge efficiency of the unpatterned and bi-tortuous electrodes was impacted by the discharge of retained brine. This is because the polyelectrolyte coatings provide incomplete coverage throughout the porous electrode thickness rather than discrete membrane layer (Fig. 1C). Since polyelectrolyte coated electrodes permit mixing between macropores and flow channel solution under galvanostatic operation, a portion of the charge stroke is associated with adsorption and release of residual brine into the flow channel. The initial dip in the cumulative SAC curves is attributed to the release and subsequent desalination of residual brine from the discharge stroke (Fig. 3 B, D and F). Desalination of salt residue in the flow channel and electrode pores can contribute to significant losses in charge and flow efficiency (Shang et al., 2017).

The differences in hydraulic residence times is likely responsible for the disparity in flow efficiency observed between UP and BT at higher current densities (Hawks et al., 2018). It is also possible that the structure of BT electrode macrochannels may have hindered mixing due to the presence of vertical channels as opposed to a planar surface. Despite flow efficiencies of 61–93% for BT:0.8 V as compared to 79–97% for UP:0.8 V, overall charge efficiency values of bi-tortuous electrodes were about 10% higher due to a longer charging times and higher rates of adsorption. Bi-tortuous electrodes demonstrate an SAC and ASAR comparable to the literature despite charge efficiency that are relatively low in comparison to MCDI (Fig. 4, Table 1) (Choi, 2015; Kim and Yoon, 2015; Kim and Choi, 2010; Zhao et al., 2012). This indicates that the adsorption capacity and rate capability of the bi-tortuous electrode CDI cells could be further increased by improving the permselectivity of the IEM coating while also maintaining the macroporous structure.

Improvements in round-trip efficiency and salt adsorption capacity of the bi-tortuous electrodes led to a four-fold increase in salt normalized energy consumption and thermodynamic efficiency (Fig. 5C–F). This increase in ENAS and $\eta_{TE}$ values with energy recovery elucidates elevated round trip efficiency as a key benefit of BT electrode macrostructures and reinforcing the importance of developing effective strategies for energy recovery (Chen et al., 2018; Długołęcki and van der Wal, 2013; Tan et al., 2018). Even when energy recovery is excluded, bi-tortuous electrodes demonstrated higher ENAS values than several previously published reports for MCDI (Długołęcki and van der Wal, 2013; Kim and Choi, 2010; Liu et al., 2014; Zhao et al., 2013b) and Ft-CDI (Hemmatifar et al., 2016; Qu et al., 2016), enforcing the importance connection between internal resistance and specific energy consumption (Table 1).

The highest thermodynamic efficiency was observed for BT-0.8 V and BT-1.0 V at 10–15 A $m^{-2}$ (Fig. 5E and F), as compared to the peak ENAS, which was observed for the lowest current density (Fig. 5C and D). While ENAS only decreases with increases in current density, thermodynamic efficiency peaks at 10 and 15 A $m^{-2}$ for the unpatterned and bi-tortuous charged at 0.8 V and follows the trend shown by a previous study for CDI (Hemmatifar et al.,

**Table 1**
Comparison of current study with previously published literature for constant current operation for Fb-MCDI and Ft-CDI. Unreported metrics are marked as '-'. The varied performances for all the studies are because of varied operational conditions, cell architectures, and flow rates.

| fb-MCDI with discrete membranes | | | | | | | | |
|---|---|---|---|---|---|---|---|---|
| Current Density (A $m^{-2}$) | [NaCl] (mM) | Q (mL $min^{-1}$) | Cut-off voltage (V) | SAC (mg $g^{-1}$) | ASAR (mg $g^{-1}$ $min^{-1}$) | $\eta_{CE}$ (%) | ENAS (μmol $J^{-1}$) | Ref. |
| 5–25 | 50 | 0.2 | 1.2 | 9.2–17 | 0.46–1.6 | 50–67 | 23–34 | Present study (BT:1.2V) |
| 5–25 | 50 | 0.2 | 0.8 | 4.1–9.7 | 0.45–1.1 | 35–67 | 27–69 | Present study (BT:0.8 V) |
| 5–25 | 50 | 0.2 | 0.8 | 2.4–6.8 | 0.36–0.94 | 33–59 | 13–46 | Present study (UP:0.8 V) |
| 37 | 40 | 30 | 1.5 | 6.54 | – | 0.78 | 17 | (Zhao et al., 2013a) |
| 38 | 40 | 60 | 1.6 | 6.3 | – | 77–81 | 12 | (Zhao et al., 2012) |
| 37 | 20 | 60 | 1.6 | 5.84 | 1.5 | – | – | (Zhao et al., 2013b) |
| 6.7–83 | 50 | 2 | 1.2 | 11–23 | 6.0–0.66 | 104 | – | (Kim and Yoon, 2015) |
| 10 | 10 | 20 | 0.8 | 6.1 | - | 96 | 40 | (Choi, 2015) |
| fte-CDI | | | | | | | | |
| 13 | 100 | 0.24 | – | 3.0–5.2 | – | – | 25–10 | (Qu et al., 2016) |

**Table 2**
Comparison of desalination performance metrics between uncoated and coated electrodes both for un-patterned and bi-tortuous electrodes at the current density of 10 A $m^{-2}$ and cut-off voltage of 0.8 V.

| Electrode type | SAC (mg $g^{-1}$) | ASAR (mg $g^{-1}$ $min^{-1}$) | $\eta_{CE}$ (%) | ENAS* (μmol $J^{-1}$) | ENAS (μmol $J^{-1}$) | $\eta_{RTE}$ (%) |
|---|---|---|---|---|---|---|
| UP Uncoated | 1.0 ± 0.03 | 0.066 ± 0.002 | 15 ± 0.5 | 3.40 ± 0.12 | 10.0 ± 0.8 | 65 ± 01.8 |
| BT Uncoated | 1.2 ± 0.15 | 0.076 ± 0.01 | 17 ± 2 | 4.04 ± 0.52 | 12.7 ± 1.8 | 68 ± 0.8 |
| UP Coated | 5.6 ± 0.05 | 0.66 ± 0.006 | 55 ± 0.5 | 12.1 ± 0.14 | 41.5 ± 1.1 | 71 ± 0.5 |
| BT Coated | 8.1 ± 0.12 | 0.79 ± 0.01 | 60 ± 0.8 | 14.0 ± 0.19 | 68.6 ± 0.9 | 80 ± 0.2 |

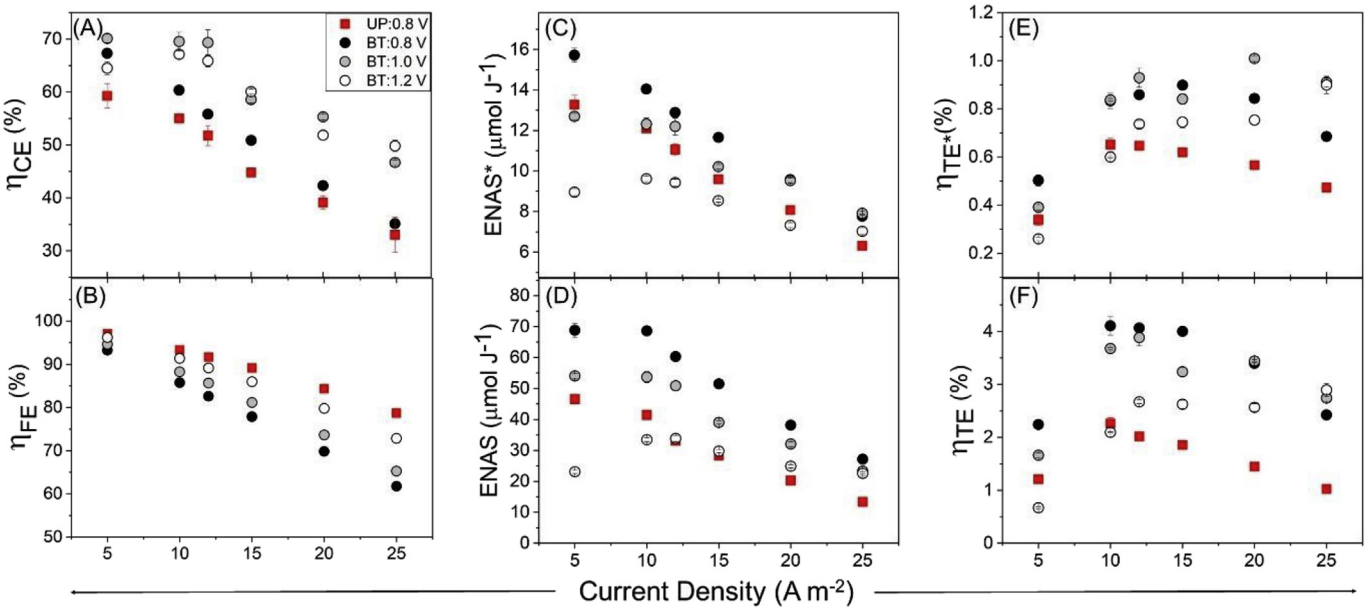


**Fig. 5.** (A) Charge efficiency ($\eta_{CE}$), (B) Flow efficiency ($\eta_{FE}$), (C) energy normalized adsorbed salt (ENAS) without and (D) with energy recovery, (E) thermodynamic efficiency ($\eta_{TE}$) without energy recovery and (F) with energy recovery as a function of current density for un-patterned (UP) and bi-tortuous (BT) electrodes.

2018). This is because resistive energy losses dominate at high current densities and faradaic energy losses dominate at lower current densities. These losses lower the thermodynamic efficiency at high and low currents respectively, leading to a peak at an optimal current density. The thermodynamic efficiencies measured in the current study compare favorably with previous reports (Table 1). A previously reported study demonstrates thermodynamic efficiencies of 2.3–2.7% with recovery for various current conditions between 1.7 and 10.2 A $m^{-2}$ for an MCDI stack reactor (Długołęcki and van der Wal, 2013), while the present study shows a higher thermodynamic efficiency (>4%) for a similar current density of 10 A $m^{-2}$ (Fig. 5F). A recent study reported a maximum thermodynamic efficiency of 9% for a traditional CDI when significant efforts are made to minimize contact resistance (Hemmatifar et al., 2018) indicating the possibility of further enhancing the performance of BT electrodes. The contrast of exceptionally high ENAS and fairly low thermodynamic efficiency is likely attributed to the feeding rate and influent concentration used in this study, which led to low thermodynamic separation minimums (Eq. (10)).

## 4. Conclusions

Bi-tortuous electrodes demonstrate lower equivalent series resistance in the tested range of current densities. Improvements in this key, but rarely reported circuit parameter translated to improved capacitance and higher energy recovery at all current densities. Reduced electrode tortuosity also increased the rate of salt adsorption, and when coupled to higher energy recovery, led to a four-fold increase in thermodynamic efficiency. Uncoated bi-tortuous electrodes performed significantly worse than polyelectrolyte coated electrodes, demonstrating that ion-exchange coatings were necessary to promote counter-ion flux. A limitation of this approach was the use of polyelectrolyte coating, which led to charge efficiencies that are lower than MCDI systems. These coatings result in a reverse-ion flux, faradaic reactions, and CDI-like diffusion limitations as opposed to an MCDI system with discrete membranes, an indication that future work should focus on depositing discrete IEM coatings onto BT electrodes. In summary, the heightened performance of fb-CDI with coated BT electrodes elucidates that both ESR and $\eta_{CE}$ are key indicators of energy efficiency desalination.

## Declaration of interest

None of the authors have any financial or personal relationships with people or organizations that could inappropriately influence this work.

## Acknowledgements

This research was funded by the US National Science Foundation [Award No. 1605290] entitled “SusChEM: Increasing Access to Sustainable Freshwater Resources with Membrane Capacitive Deionization.” APB was also supported by the Ravindar K. and Kavita Kinra Fellowship in Environmental Engineering. MDC was supported by a Fulbright Fellowship.

## Appendix A. Supplementary data

Supplementary data to this article can be found online at https://doi.org/10.1016/j.wroa.2019.100027.

## References


Ahualli, S., Iglesias, G.R., Fernández, M.M., Jiménez, M.L., Delgado, Á.V., 2017. Use of soft electrodes in capacitive deionization of solutions. Environ. Sci. Technol. 51, 5326–5333. https://doi.org/10.1021/acs.est.6b06181.

Anderson, M.A., Cudero, A.L., Palma, J., 2010. Capacitive deionization as an electrochemical means of saving energy and delivering clean water. Comparison to present desalination practices: will it compete? Electrochim. Acta 55, 3845–3856. https://doi.org/10.1016/j.electacta.2010.02.012.

Bae, C.-J., Erdonmez, C.K., Halloran, J.W., Chiang, Y.-M., 2013. Design of battery electrodes with dual-scale porosity to minimize tortuosity and maximize performance. Adv. Mater. 25, 1254–1258. https://doi.org/10.1002/adma.201204055.

Biesheuvel, P.M., 2009. Thermodynamic cycle analysis for capacitive deionization. J. Colloid Interface Sci. 332, 258–264. https://doi.org/10.1016/j.jcis.2008.12.018.

Biesheuvel, P.M., van der Wal, A., 2010. Membrane capacitive deionization. J. Membr. Sci. 346, 256–262. https://doi.org/10.1016/j.memsci.2009.09.043.

Bouhadana, Y., Avraham, E., Soffer, A., Aurbach, D., 2010. Several basic and practical aspects related to electrochemical deionization of water. AIChE J. 56, 779–789. https://doi.org/10.1002/aic.12005.

Chen, L., Yin, X., Zhu, L., Qiu, Y., 2018. Energy recovery and electrode regeneration under different charge/discharge conditions in membrane capacitive deionization. Desalination 439, 93–101. https://doi.org/10.1016/j.desal.2018.04.012.

Choi, J.-H., 2015. Comparison of constant voltage (CV) and constant current (CC) operation in the membrane capacitive deionisation process. Desalination and Water Treatment 56, 921–928. https://doi.org/10.1080/19443994.2014.942379.

Cobb, C.L., Blanco, M., 2014. Modeling mass and density distribution effects on the performance of co-extruded electrodes for high energy density lithium-ion batteries. J. Power Sources 249, 357–366. https://doi.org/10.1016/j.jpowsour.2013.10.084.

Cobb, C.L., Solberg, S.E., 2017. Communication—analysis of thick Co-extruded cathodes for higher-energy-and-power lithium-ion batteries. J. Electrochem. Soc. 164, A1339–A1341. https://doi.org/10.1149/2.0101707jes.

Cusick, R.D., Hatzell, M., Zhang, F., Logan, B.E., 2013. Minimal RED cell pairs markedly improve electrode kinetics and power production in microbial reverse electrodialysis cells. Environ. Sci. Technol. 47, 14518–14524. https://doi.org/10.1021/es4037995.

Długołęcki, P., van der Wal, A., 2013. Energy recovery in membrane capacitive deionization. Environ. Sci. Technol. 47, 4904–4910. https://doi.org/10.1021/es3053202.

Długołęcki, P., Ogonowski, P., Metz, S.J., Saakes, M., Nijmeijer, K., Wessling, M., 2010. On the resistances of membrane, diffusion boundary layer and double layer in ion exchange membrane transport. J. Membr. Sci. 349, 369–379. https://doi.org/10.1016/j.memsci.2009.11.069.

Dykstra, J.E., Porada, S., Wal, A. van der, Biesheuvel, P.M., 2018. Energy consumption in capacitive deionization – constant current versus constant voltage operation. Water Research 143, 367–375. https://doi.org/10.1016/j.watres.2018.06.034.

Dykstra, J.E., Zhao, R., Biesheuvel, P.M., van der Wal, A., 2016. Resistance identification and rational process design in capacitive deionization. Water Research 88, 358–370. https://doi.org/10.1016/j.watres.2015.10.006.

Gao, X., Porada, S., Omosebi, A., Liu, K.-L., Biesheuvel, P.M., Landon, J., 2016. Complementary surface charge for enhanced capacitive deionization. Water Research 92, 275–282. https://doi.org/10.1016/j.watres.2016.01.048.

García-Quismondo, E., Santos, C., Soria, J., Palma, J., Anderson, M.A., 2016. New operational modes to increase energy efficiency in capacitive deionization systems. Environ. Sci. Technol 50, 6053–6060. https://doi.org/10.1021/acs.est.5b05379.

Guyes, E., Simanovski, A., Suss, M.E., 2017. Several orders of magnitude increase in the hydraulic permeability of flow-through capacitive deionization electrodes via laser perforations. RSC Adv. 7, 21308–21313. https://doi.org/10.1039/C7RA00459A.

Han, L., Karthikeyan, K.G., Gregory, K.B., 2015. Energy consumption and recovery in capacitive deionization using nanoporous activated carbon electrodes. J. Electrochem. Soc. 162, E282–E288. https://doi.org/10.1149/2.0431512jes.

Hawks, S.A., Knipe, J.M., Campbell, P.G., Loeb, C.K., Hubert, M.A., Santiago, J.G., Stadermann, M., 2018. Quantifying the flow efficiency in constant-current capacitive deionization. Water Res. 129, 327–336. https://doi.org/10.1016/j.watres.2017.11.025.

Hemmatifar, A., Palko, J.W., Stadermann, M., Santiago, J.G., 2016. Energy breakdown in capacitive deionization. Water Res. 104, 303–311. https://doi.org/10.1016/j.watres.2016.08.020.

Hemmatifar, A., Ramachandran, A., Liu, K., Oyarzun, D.I., Bazant, M.Z., Santiago, J.G., 2018. Thermodynamics of Ion Separation by Electrosorption arXiv:1803.11532 [physics].

Kim, Y.-J., Choi, J.-H., 2010. Enhanced desalination efficiency in capacitive deionization with an ion-selective membrane. Separ. Purif. Technol. 71, 70–75. https://doi.org/10.1016/j.seppur.2009.10.026.

Kim, T., Yoon, J., 2015. CDI ragone plot as a functional tool to evaluate desalination performance in capacitive deionization. RSC Adv. 5, 1456–1461. https://doi.org/10.1039/C4RA11257A.

Kim, D.-H., Choi, Y.-E., Park, J.-S., Kang, M.-S., 2019a. Capacitive deionization employing pore-filled cation-exchange membranes for energy-efficient removal of multivalent cations. Electrochim. Acta 295, 164–172. https://doi.org/10.1016/j.electacta.2018.10.124.

Kim, M., Cerro, M. del, Hand, S., Cusick, R.D., 2019b. Enhancing capacitive deionization performance with charged structural polysaccharide electrode binders. Water Res. 148, 388–397. https://doi.org/10.1016/j.watres.2018.10.044.

Lee, J.-B., Park, K.-K., Eum, H.-M., Lee, C.-W., 2006. Desalination of a thermal power plant wastewater by membrane capacitive deionization. Desalination 196, 125–134. https://doi.org/10.1016/j.desal.2006.01.011.

Li, H., Zou, L., 2011. Ion-exchange membrane capacitive deionization: a new strategy for brackish water desalination. Desalination 275, 62–66. https://doi.org/10.1016/j.desal.2011.02.027.

Li, H., Gao, Y., Pan, L., Zhang, Y., Chen, Y., Sun, Z., 2008. Electrosorptive desalination by carbon nanotubes and nanofibres electrodes and ion-exchange membranes. Water Res. 42, 4923–4928. https://doi.org/10.1016/j.watres.2008.09.026.

Liu, Y., Pan, L., Xu, X., Lu, T., Sun, Z., Chua, D.H.C., 2014. Enhanced desalination efficiency in modified membrane capacitive deionization by introducing ion-exchange polymers in carbon nanotubes electrodes. Electrochim. Acta 130, 619–624. https://doi.org/10.1016/j.electacta.2014.03.086.

Nemani, V.P., Harris, S.J., Smith, K.C., 2015. Design of Bi-tortuous, anisotropic graphite anodes for fast ion-transport in Li-ion batteries. J. Electrochem. Soc. 162, A1415–A1423. https://doi.org/10.1149/2.0151508jes.

Porada, S., Zhao, R., van der Wal, A., Presser, V., Biesheuvel, P.M., 2013. Review on the science and technology of water desalination by capacitive deionization. Prog. Mater. Sci. 58, 1388–1442. https://doi.org/10.1016/j.pmatsci.2013.03.005.

Qu, Y., Campbell, P.G., Gu, L., Knipe, J.M., Dzenitis, E., Santiago, J.G., Stadermann, M., 2016. Energy consumption analysis of constant voltage and constant current operations in capacitive deionization. Desalination 400, 18–24. https://doi.org/10.1016/j.desal.2016.09.014.

Reale, Erik Richard, Smith, K.C., 2018. Reduction of tortuosity in porous electrodes through macropore patterning. ECS Trans 85, 133–153. https://doi.org/10.1149/08504.0133ecst.

Reale, Erik R., Smith, K.C., 2018. Capacitive performance and tortuosity of activated carbon electrodes with macroscopic pores. J. Electrochem. Soc. 165, A1685–A1693. https://doi.org/10.1149/2.0601809jes.

Remillard, E.M., Shocron, A.N., Rahill, J., Suss, M.E., Vecitis, C.D., 2018. A direct comparison of flow-by and flow-through capacitive deionization. Desalination 444, 169–177. https://doi.org/10.1016/j.desal.2018.01.018.

Shang, X., Cusick, R.D., Smith, K.C., 2017. A combined modeling and experimental study assessing the impact of fluid pulsation on charge and energy efficiency in capacitive deionization. J. Electrochem. Soc. 164, E536–E547. https://doi.org/10.1149/2.0841714jes.

Suss, M.E., Baumann, T.F., Bourcier, W.L., Spadaccini, C.M., Rose, K.A., Santiago, J.G., Stadermann, M., 2012. Capacitive desalination with flow-through electrodes. Energy Environ. Sci. 5, 9511–9519. https://doi.org/10.1039/C2EE21498A.

Suss, M.E., Porada, S., Sun, X., Biesheuvel, P.M., Yoon, J., Presser, V., 2015. Water desalination via capacitive deionization: what is it and what can we expect from it? Energy Environ. Sci. 8, 2296–2319. https://doi.org/10.1039/C5EE00519A.

Tan, C., He, C., Tang, W., Kovalsky, P., Fletcher, J., Waite, T.D., 2018. Integration of photovoltaic energy supply with membrane capacitive deionization (MCDI) for salt removal from brackish waters. Water Res. 147, 276–286. https://doi.org/10.1016/j.watres.2018.09.056.

Thorat, I.V., Stephenson, D.E., Zacharias, N.A., Zaghib, K., Harb, J.N., Wheeler, D.R., 2009. Quantifying tortuosity in porous Li-ion battery materials. J. Power Sources 188, 592–600. https://doi.org/10.1016/j.jpowsour.2008.12.032.

Zhang, C., He, D., Ma, J., Tang, W., Waite, T.D., 2019. Comparison of faradaic reactions in flow-through and flow-by capacitive deionization (CDI) systems. Electrochimica Acta 299, 727–735. https://doi.org/10.1016/j.electacta.2019.01.058.

Zhao, R., Biesheuvel, P.M., Miedema, H., Bruning, H., van der Wal, A., 2010. Charge efficiency: a functional tool to probe the double-layer structure inside of porous electrodes and application in the modeling of capacitive deionization. J. Phys. Chem. Lett. 1, 205–210. https://doi.org/10.1021/jz900154h.

Zhao, R., Biesheuvel, P.M., Wal, A. van der, 2012. Energy consumption and constant current operation in membrane capacitive deionization. Energy Environ. Sci. 5, 9520–9527. https://doi.org/10.1039/C2EE21737F.

Zhao, R., Porada, S., Biesheuvel, P.M., van der Wal, A., 2013a. Energy consumption in membrane capacitive deionization for different water recoveries and flow rates, and comparison with reverse osmosis. Desalination 330, 35–41. https://doi.org/10.1016/j.desal.2013.08.017.

Zhao, R., Satpradit, O., Rijnaarts, H.H.M., Biesheuvel, P.M., van der Wal, A., 2013b. Optimization of salt adsorption rate in membrane capacitive deionization. Water Res. 47, 1941–1952. https://doi.org/10.1016/j.watres.2013.01.025.